SAND2019-14685B

Encyclopedia of RF and Microwave Engineering

Kai Chang aff-0001

Texas A&M University College Station
TX

USA

Ring Resonators and Circuits

Lung-Hwa Hsieh [1]

Kai Chang [2]

[1] Sandia National Labs Albuquerque New Mexico

[2] Texas A&M University Department of Electrical Engineering College Station
Texas

Indexing terms—ring resonators

field analyses

transmission-line models

ring filters

ring couplers and hybrids

ring antennas

ring oscillators

Abstract

Because of their advantages of low cost and easy fabrication, ring resonators are used in many applications such as filters, oscillators, mixers, baluns, hybrids, magic Ts, couplers, and antennas. In addition, they have been successfully used to measure the phase velocity and dispersion of a microstrip line. This article explains the basic field and circuit model analyses that can be used to investigate the characteristics of a ring resonator. On the basis of these analyses, ring resonators can be implemented and designed for different devices. The simple structure and high performance of a ring circuit fulfill the highly desired requirements of many modern wireless systems and other applications.

1 Introduction

The dielectric constant is one of important properties when designing printed-circuit-board (PCB) circuits. When designing high frequency circuits on PCB, the properties of effective dielectric constant and dispersion effect become more crucial. The microstrip ring resonator is one of the most reliable methods to calculate the effective dielectric constant, dissipation, and dispersion effect of the circuits on a PCB. In 1969, P. Troughton used a microstrip ring resonator to measure the phase velocity and dispersion characters of a microstrip line which also can be used to determine the properties of the material of a PCB [1].

To understand the properties of a ring resonator, some complicated field analyses based on electromagnetic field theory were developed [2]. In addition, simple transmission-line analyses were also proposed [3–5]. In the transmission-line approaches, the ring resonator is modeled as equivalent circuits or equivalent lumped elements to overcome the field theory

limitation described by dimensions and mode charts of the ring resonator. These either complicate or simplified analyses provide a basic view for the ring resonator. The end result of these analyses provide circuit designers a simple equation to use for different application such as filers, antennas, oscillator…etc.

Different types of ring resonators such as microstrip, coplanar waveguide, dielectric, and slotline ring resonators were used to incorporate passive and active devices in MIC and MMIC [6–8]. A waveguide ring resonator is generally used for the applications need higher Q values and higher power handling [9]. With the advantages of compact size, low cost, easy fabrication, and low radiation loss, the planar ring resonator was widely used for the design of filters, oscillators, mixers, baluns, hybrids, magic T, couplers, frequency-selective surfaces, and antennas [10].

2 Analysis and Modeling of Ring Resonators

2.1 Field Analyses

The magnetic wall model introduced by Wolff and Knoppik was the most commonly used field theory to explain the operation of the ring resonator [2]. This model including the curvature effects of the microstrip line can achieve an accurate expression for the physical size of the ring resonator corresponding to its electric characteristics. Also, using this analysis, Wolff and Knoppik obtained a good agreement for experiment and theoretical results in the resonant frequencies of the ring.

The ring resonator shown in Fig. 1a can be treated as a cavity resonator with electric walls on the top and bottom and magnetic walls on its sides. The electromagnetic fields are confined to the dielectric substrate between the ground plane and the ring resonator conductors. Assuming no z dependency ($\partial/\partial z=0$), the fields are transverse magnetic (TM) in the z direction.

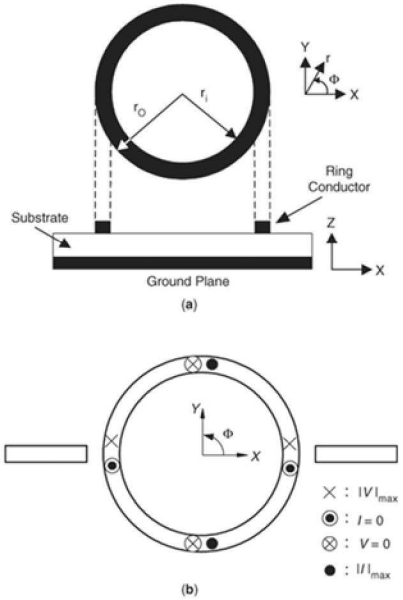

Figure 1
Ring resonator (a) configuration and (b) maximum and minimum field points.

A solution of Maxwell's equations is

$$E_z = [AJ_n(kr) + BN_n(kr)]\cos(n\Phi) \quad (1a)$$

$$H_r = \frac{n}{j\omega\mu_o r}[AJ_n(kr) + BN_n(kr)]\sin(n\Phi) \quad (1b)$$

$$H_\Phi = \frac{k}{j\omega\mu_o}[AJ_n'(kr) + BN_n'(kr)]\cos(n\Phi) \quad (1c)$$

where A and B are constants, k is the wave number, ω is the angular frequency, J_n and N_n are the Bessel function of the first and second kind of order n, and J_n' and N_n' are the derivative of the Bessel function with respect to the argument kr. With the boundary conditions $H_\Phi\big|_{r=r_o} = 0$ and $H_\Phi\big|_{r=r_i} = 0$, the eigenfunction derived from Eq. 1a, 1b and 1c is

$$J_n'(kr_o)N_n'(kr_i) - J_n'(kr_i)N_n'(kr_o) = 0 \quad (2)$$

where r_o and r_i are the outer and inner radii of the ring and $k = \omega\sqrt{\varepsilon_o\varepsilon_r\mu_o}$.
As r_i approaching to r_o, the eigenfunction in Eq. 2 reduce to [11]

$$[(kr_o)^2 - n^2][J_{n-1}(kr_o)N_n(kr_o) - J_n(kr_o)N_{n-1}(kr_o)] = 0. \quad (3)$$

The second term of Eq. 3 is nonzero, and thus

$$[(kr_o)^2 - n^2] = 0. \quad (4)$$

Substituting $k = 2\pi/\lambda_g$ into Equation (4), it yields the well-known equation

$$n\lambda_g = 2\pi r_o. \quad (5)$$

Furthermore, a planar waveguide mode considering the fringe edge effects of the microstrip line was proposed to improve the magnetic-wall model [12]. Beyond the magnetic-wall model, some rigorous solutions for the ring resonator were also reported [13].

2.2 Transmission-Line Models

The field theory for the ring resonator was introduced by Wolff and Knoppik [2]. They used the magnetic-wall model to describe the curvature effect on the resonant frequency of the ring resonator. Furthermore, based on this model, Wu and Rosenbaum found the mode chart or frequency modes [11] of the ring resonator obtained from the eigen-function of Maxwells equations with the boundary conditions of the ring. Specifically, they found the mode frequencies satisfying $2\pi r = n\lambda_g$, with n = 1,2,3, where r is the mean radius of the ring resonator, n is the mode number and λ_g is the guided-wavelength.

So far, only the annular ring resonator has the theory derivation for its frequency modes. For the square ring resonator, it is difficult to use the magneticwall model to obtain the frequency modes of the square ring resonator because of its complex boundary conditions.

Thus, in [11], the square ring resonator with complex boundary conditions was treated as a special case of an annular ring resonator, but it is not a rigorous approach.

A simple transmission-line model is used to calculate frequency modes of ring resonators of any general shape.

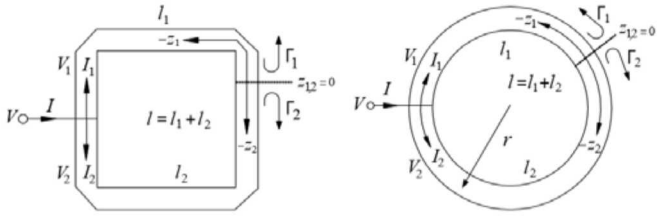

Fig. 2. The configuration of one-port annular ring resonator. (Permission from Wiley.)

Fig. 2 shows the configurations of the one-port annular ring resonators. For a ring resonator of any general shape, the total length l may be divided into l_1 and l_2 sections. each section is considered to be a transmission line. z_1 and z_2 are the coordinates corresponding to sections l_1 and l_2, respectively. The ring resonator is fed by the source voltage V at somewhere with $z_{1,2}<0$. The positions of the zero point of $z_{1,2}$ and the voltage V are arbitrarily chosen on the ring. For a lossless transmission line, the voltages and currents for the two sections are given as follows:

$$V_{1,2}(z_{1,2}) = V_0^+\left(e^{-j\beta z_{1,2}} + \Gamma_{1,2}(0)e^{j\beta z_{1,2}}\right) \tag{6a}$$

$$I_{1,2}(z_{1,2}) = \frac{V_0^+}{z_0}\left(e^{-j\beta z_{1,2}} - \Gamma_{1,2}(0)e^{j\beta z_{1,2}}\right) \tag{6b}$$

where $V_0^+ e^{-j\beta z_{1,2}}$ is the incident wave propagating in the $+z_{1,2}$ direction, $V_0^+\Gamma_{1,2}(0)e^{j\beta z_{1,2}}$ is the reflected wave propagating in the the $-z_{1,2}$ direction, β is the propagation constant, Γ is the reflection coefficient at $+z_{1,2} = 0$ and z_o is the characteristic impedance of the ring.

When a resonance occurs, standing waves set up on the ring. The shortest length of the ring resonator that supports these standing waves can be obtained from the positions of the maximum values of these standing waves. These positions can be calculated from the derivatives of the voltages and currents in (6). The derivatives of the voltages are

$$\frac{\partial V_{1,2}(z_{1,2})}{\partial z_{1,2}} = -j\beta V_0^+\left(e^{-j\beta z_{1,2}} - \Gamma_{1,2}(0)e^{j\beta z_{1,2}}\right). \tag{7}$$

Letting $\frac{\partial V_{1,2}(z_{1,2})}{\partial z_{1,2}} = 0$, the reflection coefficients can be found as

$\Gamma_{1.2}(0) = 1.$ (8)

Substituting $\Gamma_{1.2}(0) = 1$ (6), the voltages and currents can be rewritten as

$$V_{1,2}(z_{1,2}) = 2V_0^+ cos(\beta z_{1,2}) \quad (9a)$$

$$I_{1,2}(z_{1,2}) = -\frac{j2V_0^+}{Z_0} sin(\beta z_{1,2}) \quad (9b)$$

Therefore, the absolute values of the maximum voltages on the ring resonator can be found as

$$\left|V_{1.2}(z_{1,2})\right|_{max} = 2V_0^+ \text{ for } z_{1,2} = m\frac{\lambda_g}{2}, \text{ m=0, -1, -2, -3, …} \quad (10)$$

In addition, the currents $I_{1,2}$ at the positions of $z_{1,2} = m\frac{\lambda_g}{2}$ are

$$I_{1,2}(z_{1,2})\big|_{z_{1,2}=m\frac{\lambda_g}{2}} = 0. \quad (11)$$

Also, the absolute values of the maximum currents can be found as

$$\left|I_{1.2}(z_{1,2})\right|_{max} = \frac{2V_0^+}{Z_0} \text{ for } z_{1,2} = \frac{(2m-1)}{4}\lambda_g, \; m = 0, -1, -2, -3, \ldots \quad (12)$$

and the voltages $V_{1,2}$ at the positions of $z_{1,2} = \frac{(2m-1)}{4}\lambda_g$ are

$$V_{1,2}(z_{1,2})\big|_{z_{1,2}=\frac{(2m-1)}{4}\lambda_g} = 0. \quad (13)$$

Fig. 3 shows the absolute values of voltage and current standing waves on each section l_1 and l_2 of the square ring resonator. Inspecting Fig. 3, the standing waves repeat for multiples of $\frac{\lambda_g}{2}$ on each section of the ring. Thus, to support standing waves, the shortest length of each section on the ring has to be $\frac{\lambda_g}{2}$, which can be treated as the fundamental mode of the ring. For higher order modes,

$$l_{1,2} = n\frac{\lambda_g}{2} \text{ for } n = 1,2,3, \ldots \quad (14)$$

where n is the mode number. Therefore, the total length of the square ring resonator is

$$l = l_1 + l_2 = n\lambda_g \quad (15)$$

or in terms of the annular ring resonator with a mean radius *r* as shown in Fig. 2,

$$l = n\lambda_g = 2\pi r \quad (16)$$

Equation (16) shows a general expression for frequency modes and may be applied to any configuration of microstrip ring resonators.

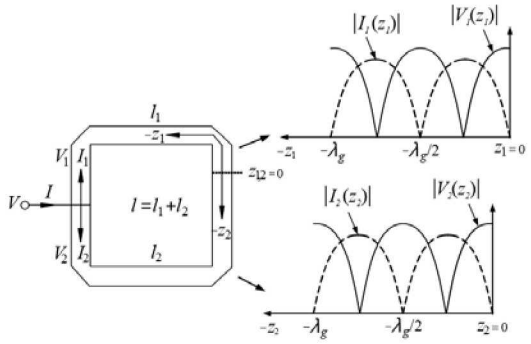

Fig. 3. Standing waves on each section of the square ring resonator. (Permission from Wiley.)

3 Measurement Using Ring Resonators

The ring resonators are widely used in measuring for dispersion, dielectric constant, and *Q* factor. As mentioned in the introduction, it is crucial for an RF designer to know the dielectric constant of the material when designing at high frequency circuit. And one of reliable methods is using a ring resonator.

The microstrip ring circuit shown in Fig. 1(b) consists of two feedlines, one closed-loop ring with two coupling gaps between the ring and the feedlines. The size of the coupling gaps should be large enough so that the coupling effects on the ring will not affect the resonant frequency. Equation 17 demonstrates that the ring supports waves with an integral multiple guided wavelengths equal to the mean circumference of the ring

$$n\lambda_g = 2\pi r\,,\ n = 1, 2, 3\ \ldots. \tag{17}$$

where n is the mode number and r is the mean radius. The dispersion in a microstrip line can be examined by the effective dielectric constant ε_{eff}. The effective dielectric constant is defined as the square of the ratio of the speed of light in free space c to the phase velocity v_p in a microstrip line:

$$\varepsilon_{eff}(f) = \left(\frac{c}{v_p}\right)^2 = \left(\frac{c}{f\lambda_g}\right)^2 = \left(\frac{\lambda_o}{\lambda_g}\right)^2 \tag{18}$$

Substituting Eq. 17 into Eq. 18 gives

$$\varepsilon_{eff}(f_o) = \left(\frac{nc}{2\pi r f_o}\right) \tag{19}$$

where f_0 is the resonant frequency. Thus, the effective dielectric constant with the dispersion of the microstrip line can be calculated from Eq. 19. The accuracy of the dispersion calculation depends on the accuracy of the measurement of the frequency and the total circumference of the ring.

A figure of merit for a ring resonator is its Q factor. The loaded Q factor of the ring can be measured by $Q_L = \frac{f_o}{f_2 - f_1}$, where f_0 is the angular resonant frequency and f_1–f_2 is the 3 dB (half-power) bandwidth. The corresponding frequency response is shown in Fig. 4. Moreover, the unloaded Q factor of the ring can be determined by measuring the loaded Q factor and the insertion loss of the ring at the resonance. The unloaded Q factor is calculated from

$$Q_u = \frac{Q_L}{\left(1 - 10^{-L/20}\right)} \tag{20}$$

where L is the insertion loss in decibels at resonance of the ring.

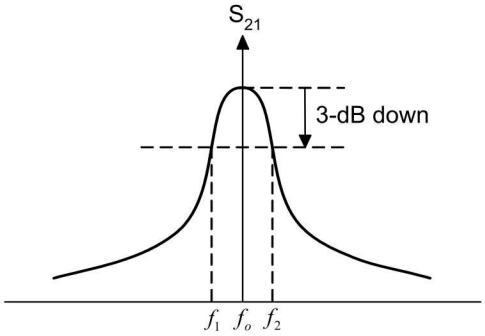

Figure 4
Frequency response of a resonator.

The unloaded Q of the ring resonator can be calculated its equivalent G, L, C parallel circuit. The G is equivalent conductance of the ring resonator, the L is the equivalent inductor of the ring resonator, the C is the equivalent capacitor of the ring resonator, α is the attenuation constant, and ω_o is the resonant angular frequency. The lumped elements G, L, and C are derived from $ABCD$, Y, and S parameters [5].

The unloaded Q of the ring resonator can be obtained as

$$Q_u = \frac{\omega_o C}{G} = \frac{\pi}{\alpha \lambda_g} \tag{21}$$

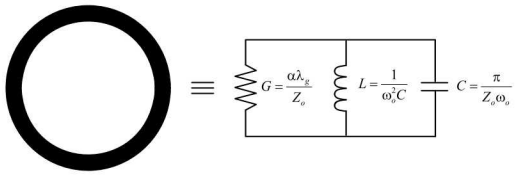

Figure 5. The ring resonator and its equivalent circuit in terms of G, L, and C.

4 Filters

One of useful applications of ring resonators is the bandpass filter. The filters can be microstrip, strip and coplanar wave-guided, patch type configurations. Among them, the micostrip ring resonators are the most popular bandpass filter configuration because of its design simplicity and good performance.

The dual mode bandpass filters were introduced by Wolff using asymmetric coupling feedlines as shown in Fig. 6 [15]. The asymmetries perturb the fields of the ring and generate two separated modes. These two modes couple each other and increase the passband of the ring resonator. The dual-mode effects are introduced by skewing one of feedlines with respect to the other, and/or by introduction of a discontinuity (notch, slit, patch, etc.) [10]. Later on, many new configurations using orthogonal feedlines with patch perturbation on a ring resonator were introduced [16–18]. The new configuration with orthogonal feedlines and a patch perturbation provides a quasielliptic function that has two transmission zeros close to the passband to reject adjacent channel interferences as shown in Fig. 7 [17]. Also, by cascading several resonators in series, various bandpass frequency responses can be designed [19].

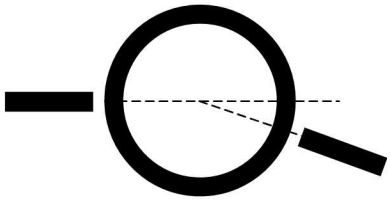

Figure 6
Asymmetrically coupling ring resonator.

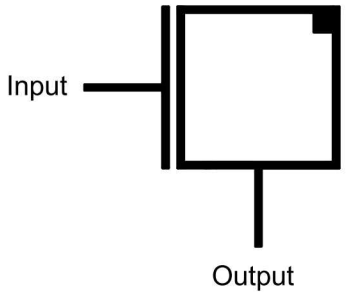

Figure 7
A dual-mode ring circuit with one single coupling gap [17]. (Permission from Electronics Letters.)

To reduce the size of the filters, engineers start to use open-loop ring resonators to design filters. This type filter has good performance at insertion loss and out-of-band rejections. Fig 8 shows an open-loop ring resonator filters. By using asymmetrically feeding on the two open-loop ring resonators provides two transmission zeros [20]. In comparison with the cross-coupled structure of Ref. [21], this configuration using only two resonators can also provide a sharp cutoff frequency response but has lower insertion loss due to fewer conductor losses.

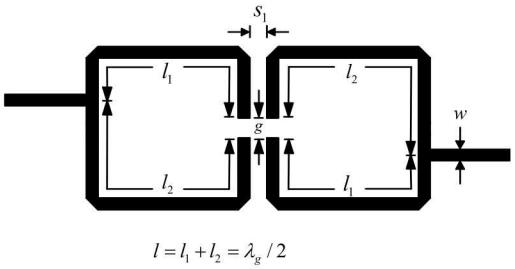

Figure 8
Layout of the filter using two open-loop ring resonators with asymmetric tapping feeders [20]. (Permission from IEEE.)

In Fig. 8, the total length of the resonator is $l = l_1 + l_2 = \lambda_g / 2$, and the input and output feeders divide the resonators into two sections of l_1 and l_2, where λ_g is the guided wavelength. By using *ABCD*, *Y*, and *S* parameter operations, the locations of the transmission zeros corresponding to the tapping position on the ring resonator are given by

$$f_1 \cong \frac{nc}{4l_1\sqrt{\varepsilon_{eff}}} \quad \text{and} \quad f_2 \cong \frac{nc}{4l_2\sqrt{\varepsilon_{eff}}} \qquad n = 1,\ 3,\ 5... \tag{22}$$

To verify the calculation from Eq. 17, a filter was designed at the fundamental frequency of 2 GHz and fabricated on a RT/Duroid 6010.2 substrate with a thickness h=25 mil and a relative dielectric constant $\varepsilon_r = 10.2$. The dimensions of the filter are g=0.5 mm, s_1=0.35 mm, l_1=12.69 mm, w=0.563 mm, and l_2=16.16 mm. The measured results are shown in Fig. 12. The calculated and measured results shown in Table 4 agree well. The filter has an insertion loss of 0.95 dB at 2.02 GHz, return loss of greater than 20 dB from 1.98 to 2.06 GHz, and two transmission zeros at 1.69 GHz with −50.7 dB rejection and 2.5 GHz with −45.5 dB rejection, respectively. The 3 dB fractional bandwidth of the filter is 10.4%.

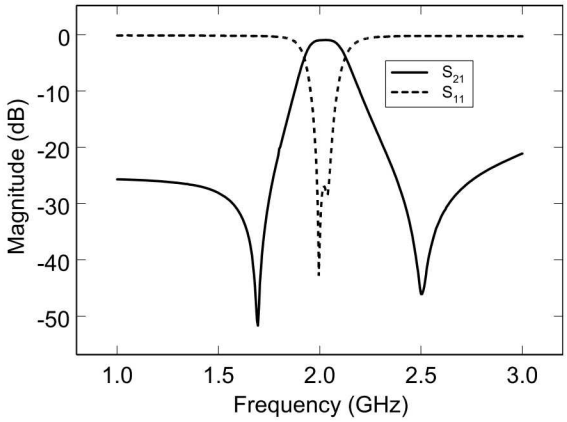

Figure 8
Measured results of the filter [20]. (Permission from IEEE.)

Table 1 Calculated and Measured Locations of Two Transmission Zeros

Calculation	Measurements
f_1=1.79 GHz, f_2=2.27 GHz	f_1=1.83 GHz, f_2=2.24 GHz

Figure 9 [22] shows the parallel dual-band bandpass filter. The dual-band filter consists of two different bandpass filters indicated by the two rectangular boxes, the microstrip lines with the lengths of l_1 and l_2 and the impedance of Z_0. Z_{in1} and Z_{in2} are the input impedances looking into the transmission lines of l_1 and l_2 and the bandpass filters. Considering the input impedances of Z_{in1} and Z_{in2} for the passbands and stopbands shown in Figure 1, if Z_{in2} (Z_{in1}) is infinite at f_{01} (f_{02}), then the dual-band bandpass filter passes the passband at BFP1 (BFP2) and blocks the passband at BFP2 (BFP1).

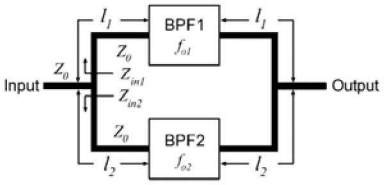

Fig. 9. The configuration of the parallel dual-band bandpass filter. (Permission from Wiley.)

Figure 10 shows more details of the dual-band bandpass filter, where Z_{l1} and Z_{l2} are the input impedances looking into BPF1 and BPF2.

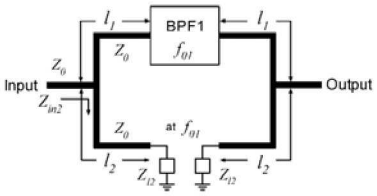

(a)

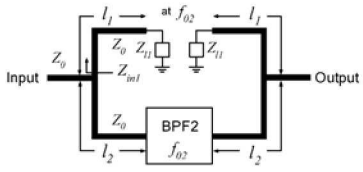

(b)

Fig. 10. The dual-band bandpass filter: (a) passband at f_{01} and (b) passband at f_{02}. (Permission from Wiley.)

The input impedance of Z_{in2} can be expressed as

$$Z_{in2} = Z_0 \frac{Z_{l2}+jZ_0 tan(\beta l_2)}{Z_0+jZ_{l2} tan(\beta l_2)} \quad (23)$$

where β is the propagation constant. Letting $l_2 = \lambda_{g1}/4$, the input impedance reduces to

$$Z_{in2} = \frac{Z_0^2}{Z_{l2}} \tag{24}$$

where λ_{g1} is the guided wavelength at f_{01}. Also, letting $l_2 = \lambda_{g1}/2$, the input impedance reduces to

$$Z_{in2} = Z_{l2} \tag{25}$$

To obtain $Z_{in2} = \infty$ in Equation (24) requires $Z_{l2} = 0$, and Z_{l2} in Equation (25) requires $Z_{l2} = \infty$. In practice, obtaining ideal impedances of $Z_{l2} = 0$ and $Z_{l2} = \infty$ is not easy. However, the low and high impedances of Z_{l2} can be implemented easily using parallel and series resonators shown in Figure 11, where ω is the angular frequency, L is the inductance, and C is the capacitance.

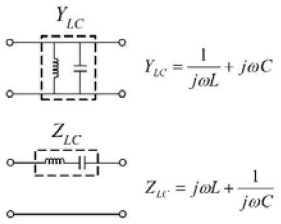

Figure 11. Equivalent circuits of the parallel and series resonators. (Permission from Wiley.)

At nonresonant frequencies, Y_{LC} and Z_{LC} show high admittance and high impedance, and at resonant frequencies, Y_{LC} and Z_{LC} show low admittance and low impedance. These low and high impedance characteristics can be used to implement the dual-band bandpass filter shown in Figure 10. For example, Figure 12 shows a dual-band bandpass filter with two parallel resonators at resonant frequencies of f_{01} and f_{02}. Considering BPF2 at the passband frequency of f_{01}, the input impedance of Z_{l2} shows low impedance and through the quarter-wavelength transformer of $l_2 = \lambda_{g1}/4$, the input impedance of Z_{in2} presents high impedance that blocks the passband at f_{01}. Similar results can be obtained for BPF1 at the passband frequency of f_{02}.

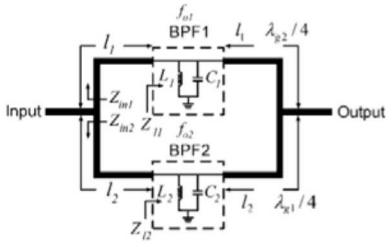

Figure 12. Daul-band bandpass filter using two parallel resonators. (Permission from Wiley.)

The dual-band bandpass filter using two open-loop ring resonators with asymmetrical feeding is shown in Figure 13. Because the open-loop ring resonator is the parallel-type resonator, it can be used to implement the dual-band bandpass filter. The filter uses two different ring resonators in parallel for passing two different bands. The asymmetrical feed structure of the filter provides sharp rejections at its adjacent passbands, which benefits the dual-band bandpass

filter when the passbands are close together. The dual-band bandpass filter shown in Figure 13 is designed at the center resonant frequencies of 1.9 and 2.4 GHz, respectively.

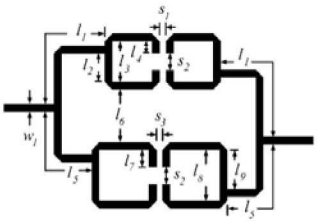

Figure. 13. The configuration of the microstrip dual-band bandpass filter. (Permission from Wiley.)

The dual-band bandpass filter was fabricated on a 50-mm-thick RT/Duroid substrate with relative dielectric constant ε_r =10.2. The dimensions of the filter are l_1 = 15 mm, l_2 = 4.3 mm, l3 = 6.1 mm, l4 = 1.76 mm, l5 = 11.8 mm, l6 = 7.9 mm, l7 = 2.53 mm, l8 = 7.6 mm, l9 = 5.8 mm, s1 = 0.96 mm, s2 = 2.54 mm, s3 = 0.91 mm, and w1 = 1.17 mm. The gap sizes of s1 and s3 are optimized for tight coupling by using a IE3D electromagnetic simulator [23].

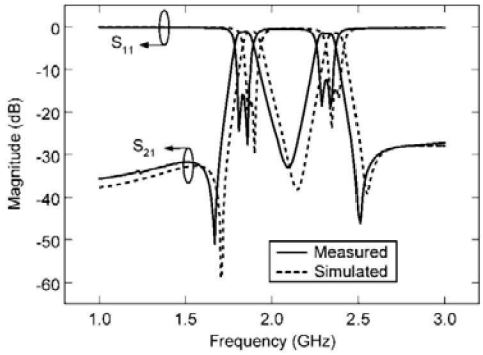

Fig. 14. The simulated and measured results of the dual-band bandpass filter. (Permission from Wiley.)

Figure 14 shows the simulated and measured results of the dual-band bandpass filter. The minimum insertion loss is 1.25 dB at 1.85 GHz and 1.6 dB at 2.33 GHz. In addition, the filter has return loss greater than 10 dB within the passband of 1.8–1.88 GHz and 2.28–2.36 GHz, respectively. The 3-dB fractional bandwidths are 5.9% for the 1.9-GHz bandpass filter and 4.7% for the 2.4-GHz bandpass filter, respectively.

5. Ring Couplers and Hybrids

Hybrid ring couplers are widely used in various microwave integrated circuit (MIC) and monolithic microwave integrated circuit (MMIC) applications such as balanced amplifiers, balanced mixers, phase shifts, frequency discriminators, and feeding networks in antenna arrays [24–27]. The 180° hybrid ring couplers and 90° branchline couplers are commonly used in these applications. Ratrace hybrid rings and reverse-phase hybrid rings are well known for

the 180° hybrid ring couplers [28, 29]. Different types of hybrid couplers using slotline and coplanar waveguide structures have also been reported [6].

Figure 15 shows a microstrip hybrid ring coupler. When a unit amplitude wave is incident at port 4 of the coupler, the wave is divided into two components at the ring junction. These two components arrive in phase at ports 2 and 3, and 180° out of phase at port 1. Furthermore, if a unit amplitude is incident at port 1 of the coupler, the wave divides into two components that arrive at ports 2 and 3 with a net phase difference of 180°, and 180° out of phase at port 4.

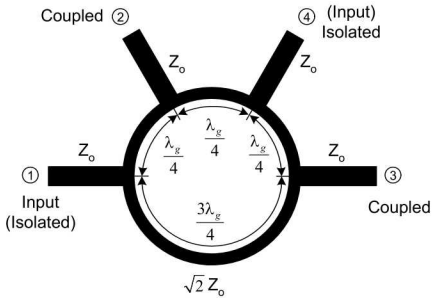

Figure 15
A microstrip hybrid ring coupler.

According to the characteristics of the coupler, a balanced mixer can be built. The single balanced mixer shown in Fig. 16 consists of a hybrid ring coupler, two diodes, two RF chokes, two DC blocks, and one lowpass filter. The local oscillator (LO) is 180° out of phase at the RF port, providing the isolation between the LO and RF ports. The LO signal is split equally but is 180° out of phase at two diodes. The RF signal is split equally and in phase into two diodes. The phase noise of LO is thus canceled. Both RF and LO signals are mixed in the diodes to generate an IF signal at the output of the lowpass filter. The RF chokes provide a tuning mechanism and prevent the RF signal from leaking into ground. Figure 17 shows the measured results of a 94-GHz hybrid coupler mixer [27]. The mixer has a conversion loss of less than 8 dB over a 3 GHz RF bandwidth using LO pump power of 8 dBm and less than 6.5 dB with LO pump power of 10 dBm.

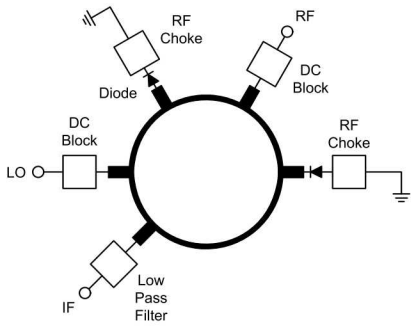

Figure 16
A hybrid coupler mixer.

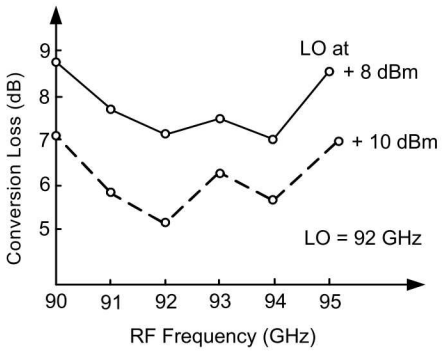

Figure 17
Performance of a 94-GHz hybrid coupler mixer [27].

6 Ring Antennas

In mid-1970s, microstrip antennas drew widespread attention because of their low cost and easy fabrication. Also, they could be easily used to design circularly polarized antennas, frequency-selective surface antennas, active antennas, phased arrays, reflect arrays, and so on [30–33]. New designs and applications of coplanar antennas are expected in modern wireless and personal communication systems.

6.1 Ring Antenna Circuit Models

The ring antenna shown in Fig. 18 consists of a close-loop ring conductor on one side of the substrate with a ground plane on the other side. The ring has an inside radius of r_i and an outside radius of r_o. The feedpoint radius is r_p. The total length of the ring antenna can be calculated from Eq. 17.

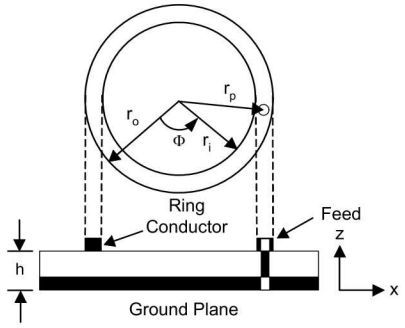

Figure 18
Configuration of a ring antenna.

Since the thickness h is very small compared to the wavelength λ_0, the variation of the electric field in the z direction can be ignored. Without the Φ dependence, the TM modes of the electric and magnetic fields of the ring antenna are given by [34]

$$E_z(r) = A_n J_n(kr) + B_n N_n(kr) \tag{26}$$

$$H_\Phi(r) = -\frac{jk}{\omega\mu_o}[A_n J_n'(kr) + B_n N_n'(kr)] \tag{27}$$

These fields are used to define modal voltages and currents. The modal voltage is simply defined as $E_z(r)$. The modal current is rH_Φ or $-rH_\Phi$ for power propagation in the r direction, respectively. The admittance at any point r is expressed by

$$Y(r) = \frac{rH_\Phi(r)}{E_z(r)} \qquad r < r \tag{28}$$

$$Y(r) = -\frac{rH_\Phi(r)}{E_z(r)} \qquad r > r_p \tag{29}$$

6.2 Slot Ring Antennas

The slot antenna is a dual version of the microstrip ring antenna; a comparison is given in Fig. 19 [35]. It has a wider impedance bandwidth than does microstrip antenna. Therefore, the bandwidth of the slot antenna is greater than that of the microstrip antenna. By introducing some asymmetry to the slot antenna, a circular polarization (CP) radiation can be obtained. The slot ring antenna in the ground plane of a microstrip transmission line can be readily made into a corporate-fed array by implementing microstrip dividers.

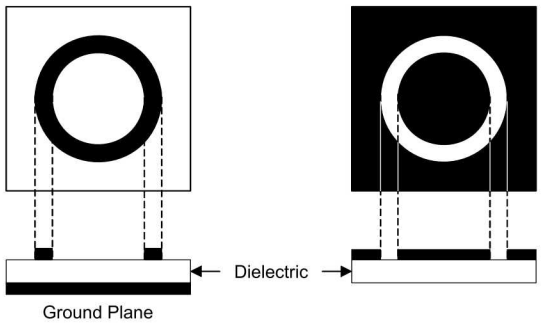

Figure 19
Comparison of (a) microstrip ring and (b) slot ring structures.

To use the structure as an antenna, the first-order mode is excited as shown in Fig. 20 [35]. Also, the impedance seen by the voltage source is real at resonance. All the power delivered to the ring will be radiated [35]. The resonant frequency can be calculated using the transmission-line model [35].

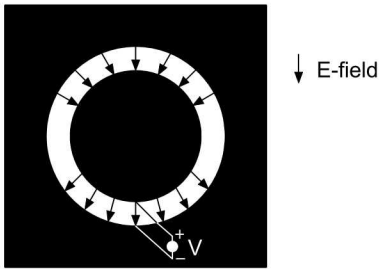

Figure 20
Slot ring feed method showing electric field.

Figure 21 shows a multifrequency annular slot antenna [36, 37]. A 50-Ω microstrip feed is electromagnetically coupled to the slot ring at point *A* and is extended to point *C*. The circuit was etched on a Keene Corporation substrate with relative dielectric constant of 2.45 and height of 0.762 mm. The widths of the microstrip (w_m) and slot ring (w_s) were 2.16 and 2.9 mm, respectively. The mean circumference of the slot ring was 93.3 mm.

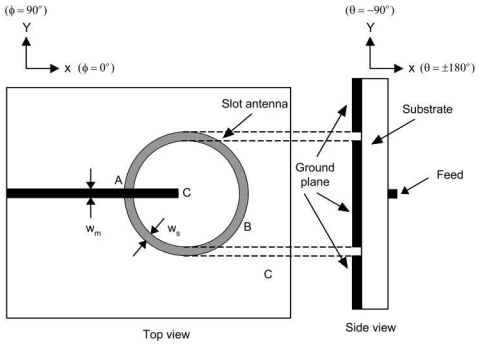

Figure 21
The configuration of the multifrequency annular antenna.

Ignoring the microstrip feed and treating the slot ring antenna as a transmission line, one expects the operating frequency to be the frequency at which the circumference of the slot ring antenna becomes one guided wavelength of the slot (λ_{gs}). A slot guided wavelength for the frequency range of interest can be obtained from [38]

$$\lambda_{gs} = \lambda_o \left\{ 1.045 - 0.365 \ln \varepsilon_r + \frac{6.3(w_s / h)\varepsilon_r^{0.945}}{(238.64 + 100 w_s / h)} - \left[0.148 - \frac{8.81(\varepsilon_r + 0.95)}{100\varepsilon_r} \right] \ln(h / \lambda_o) \right\} \quad (30)$$

where λ_0 is the free-space wavelength and h is the thickness of the substrate. At 2.97 GHz, λ_{gs} is equal to the mean circumference of the antenna (93.3 mm). From this information, as a first-order approximation, first-operating frequency of the slot ring antenna is 2.97 GHz. The actual operating frequency of the microstrip-fed slot ring antenna can be either above or below this approximate frequency depending on the length of the microstrip stub.

The return loss of the multifrequency antenna and simulation results agree well and as shown in Fig. 22. The simulation was carried out by electromagnetic simulator [23]. Defining the operating frequency to be a frequency at which return loss is less than 10 dB, these experimental operating frequencies are centered at 2.58, 3.9, 5.03, and 7.52 GHz. The measured patterns of the antenna at resonant frequency of 2.65 GHz are shown in Fig. 23.

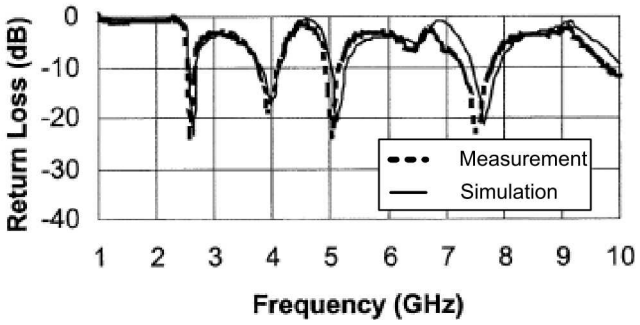

Figure 22
Measured and simulated return loss of the multifrequency antenna with AC=46.85 mm [36]. (Permission from IEEE.)

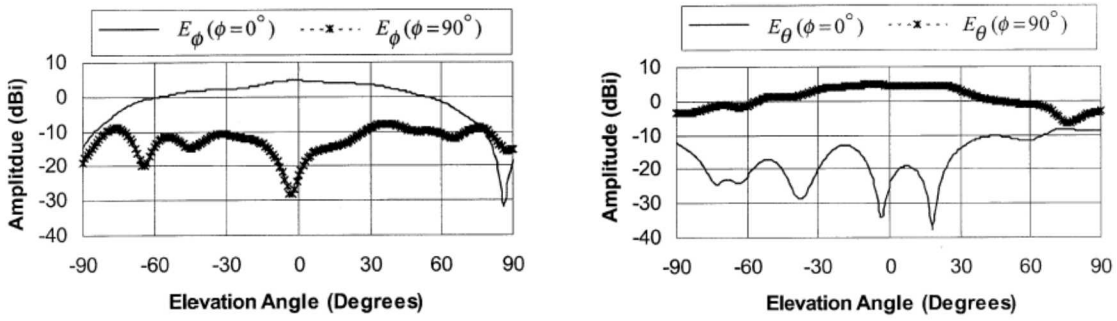

Figure 23
Radiation patterns of the multifrequency antenna with microstrip stub length AC=46.85 mm at 2.65 GHz [36]. (Permission from IEEE.)

6.3 Active Ring Antennas

Active integrated antennas have the advantages of reducing the size, weight, and cost of many transmit and receive systems. Solid-state devices can be incorporated into an antenna to provide various functions. Two- and three-terminal solid-state devices have been integrated with various antennas to form switches, tuners, detectors, mixers, amplifiers, oscillators, Doppler sensors, and receivers. The choice between transistors and diodes is not clearcut. It depends on the type of microwave component required, operating frequency range, RF power output desired, available DC power input, and other considerations. Unlike the design of a passive antenna, the design of an integrated active antenna needs to include the effects of device packages and bias lines. The effects often cause changes in operating frequencies, lower conversion efficiencies, and higher cross-polarization levels (CPLs).

As an example, the active antenna shown in Fig. 24 consists of a Gunn diode and a slotline notch antenna stabilized with a slotline ring resonator [32]. The Gunn diode is placed across the ring resonator at a low-impedance point to meet the conditions for oscillation. The slotline ring's resonant wavelength can be determined from

$2\pi r = n\lambda_g$ for $n = 1, 2, 3, \ldots$ where r is the mean radius of the slotline ring, λ_g is the guided wavelength in the slotline ring, and n is the mode number.

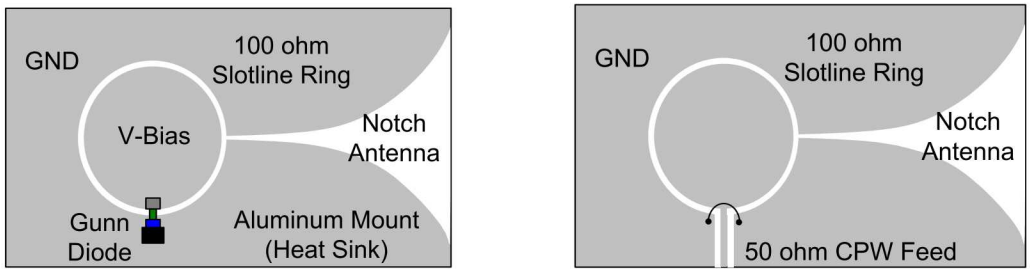

Figure 24
Configuration of active antenna (a) Gunn diode active notch antenna using a slotline ring resonator (the wire for DC bias to the center of the ring is not shown) and (b) CPW-fed passive antenna (some dimensions in the figures are exaggerated to enhance detail) [32].

Figure 24a shows the circuit configuration of the active antenna, while Fig. 24b shows the coplanar waveguide (CPW)-fed passive antenna developed for radiation pattern comparison. The antennas were etched on Duroid 5870 board with a relative dielectric constant of 2.33, substrate thickness of 62 mils (1.575 mm), and 1-oz copper metallization. The antennas are truly uniplanar, requiring no backplane for excellent performance. The slotline ring has a mean radius of 3.81 mm and a slot width of 0.18 mm. The CPW feedline in the passive antenna has a center strip width of 1.2 mm and symmetric side gaps of 0.08 mm. A thin-wire airbridge is used to operate the CPW line in the even mode. The slotline notch antenna uses an exponential taper to match the impedance of the ring to free space. The antenna length is 6 cm, and the gap at the feedpoint is 0.18 mm. The aluminum mount used in the active antenna also serves as the heatsink for the Gunn diode. The DC bias is provided directly to the center of the slotline ring. The active antenna radiates a clean spectrum at 9.26 GHz with a bias voltage of 10.0 V and draws 410 mA. The active antenna produces an effective power output of 27.1 mW and an effective isotropic radiated power (EIRP) of 720.0 mW. The spectrum has a phase noise of –95.33 dBc/Hz at 100 kHz from the carrier, while the second-harmonic radiation produced by the active antenna is 26.16 dB below the fundamental frequency. Figure 25 shows the radiation patterns of the active antenna.

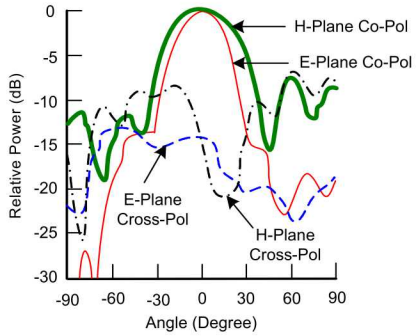

Figure 25

E-plane radiation pattern—half-power beamwidth (HPBW)=33°, cross-polarization=13.18 dB below copolarization; *H*-plane radiation pattern—HPBW=47°, cross-polarization=6.69 dB below copolarization [32].

The *E*-plane and *H*-plane patterns are smooth with cross-polarization levels of 13.18 and 6.69 dB below copolarization. The radiation *E* plane and *H* plane are 33° and 47°, respectively. The radiation pattern of the CPW-fed passive antenna is essentially similar with the exception that the cross-polarization levels are 18.74 and 16.51 or the *E* and *H* planes, respectively.

6.4 Reflect Array Using Ring Resonators

Microstrip reflectarrays have been shown to be good candidates for replacing the conventional parabolic reflector antennas. The technologies involve a flat printed array integrated with a space-feeding horn and have the advantages of low cost, low profile, easy fabrication, and flat surface [39].

Figure 26 shows the configuration of the reflectarray with a Ka-band feedhorn [33]. The reflectarray is constructed by ring resonators with two slits at the top and the bottom. Compared with the reflectarray using square patch antennas, this configuration using ring antennas can increase the operating bandwidth and reduce blockage when using in a dual-layer, dual-frequency application.

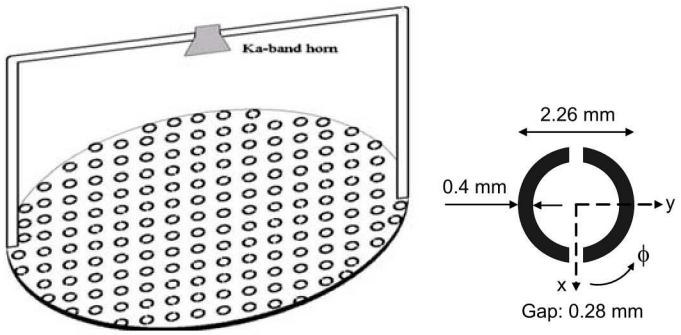

Figure 26
Configuration of Ka-band reflectarray (a) setup and (b) ring antenna [33]. (Permission from *Electronics Letters*.)

Because of the nature of reflection, an incident right-hand circularly polarized wave is reflected as a left-hand circularly polarized wave. However, by using these two slits on the ring, the reversal of polarization can be canceled out. Also, a simple trigonometric relation is used to calculate the required additional pathlengths to create a parabolic phase front across an array's surface. Each ring antenna is rotated counterclockwise by ϕ radians at each position when 2ϕ radians are needed for compensating these additional pathlengths. For the whole reflectarray with a diameter of 0.5 m, the repetitious behaviors of array configurations are found to be more than 4 times that of a 2π radian.

A 0.5-m reflectarray has been designed for broadside radiation at a focal distance of 350 mm corresponding to an *f*/*D* ratio of 0.7. The ring antennas are fabricated on RT/Duroid 5870 substrate with ε_r =2.33 and 0.508 mm thickness. The space between rings is 0.5 free-space wavelength, which is selected to avoid grating lobes. The measured results at 31.75 GHz are shown in Fig. 27. The mainbeam has a beamwidth of 1.3°. The cross-polarization level is 40.71 dB down at broadside, and the sidelobe suppression is greater than 19.47 dB, occurring at 2°. This cross-polarization level corresponds to an axial ration of less than 0.5 dB. The

relatively high peak sidelobe is due to feedhorn blockage effects. The measured efficiency of the reflectarray is shown in Fig. 26. The efficiency is better than 40% from 31.5 to 32.5 GHz. The highest efficiency is 50% at 31.75 GHz.

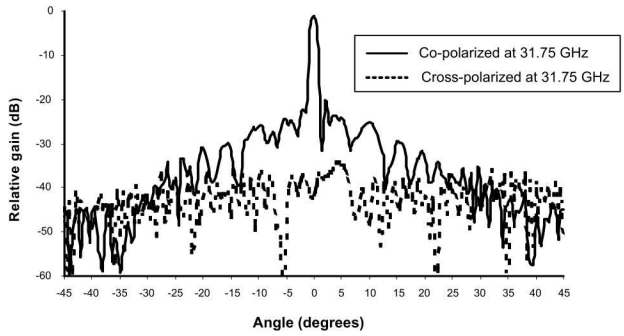

Figure 27
Measured radiation patterns [33]. (Permission from *Electronics Letters*.)

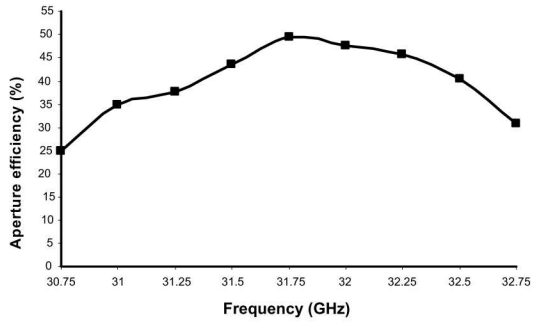

Figure 28
Measured aperture efficiency [33]. (Permission from *Electronics Letters*.)

7 Ring Oscillators

With the advantages of high Q factor, low radiation loss, low cost, and easy fabrication, the ring resonator can be used to design an oscillator. Moreover, comparing to dielectric resonator oscillators, a varactor can be easily mounted in a ring oscillator to tune the oscillation frequency [40]. Several different types of oscillators using ring resonator have been introduced [41–43].

Figure 29 shows a feedback oscillator that consists of a feedback ring circuit and a two-port negative-resistance oscillator with input and output matching networks [39]. The closed-loop ring resonator using a pair of orthogonal feedlines suppresses odd resonant frequencies and operates at even resonant frequencies. This operation is characterized by high operating resonant frequencies, similar to those of push–push oscillators [43]. Also, the high-Q ring resonator is used to reduce the noise of the two-port negative-resistance oscillator.

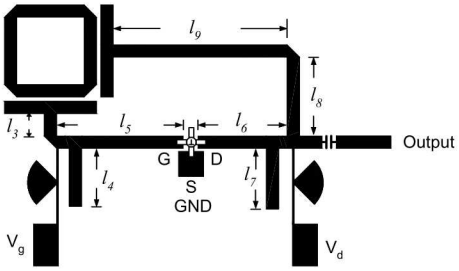

Figure 29
Feedback ring resonator oscillator [42]. (Permission from IEEE.)

The active device used is a NE32484A HEMT from NEC. The dimensions of the oscillator are l_3=3 mm, l_4=6.95 mm, l_5=15.19 mm, l_6=10.69 mm, l_7=7.3 mm, l_8=9.47 mm, and l_9=21.19 mm. The two-port negative-resistance oscillator uses the one open-end terminal as a series-feedback element to obtain a potential instability. Also, with input and output matching networks, the two-port oscillator with an applied bias of V_{gs}=−0.65 V and V_{ds}=1 V has a negative resistance around 12 GHz.

Figure 30 shows a measured spectrum of the oscillator with applied voltages of V_{gs}=−0.65 V and V_{ds}=1 V. Also, as shown in Fig. 28, the oscillator is operated at the second resonant mode of the ring resonator. The oscillator has the efficiency of 48.7% with output power of 3.41 mW at 12.09 GHz. The phase noise of the oscillator is −96.17 dBc/Hz at offset frequency of 100 kHz.

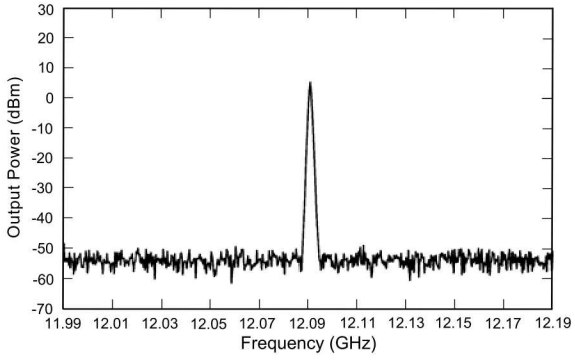

Figure 30
Output power for the feedback ring resonator oscillator operated at the second resonant mode of the ring resonator [42]. (Permission from IEEE.)

Figure 31 shows a configuration of the ring resonator oscillator integrated with a piezoelectric transducer (PET) with an attached dielectric perturber. When a DC voltage is applied to the PET, the PET moves the perturber up or down vertically to change the effective dielectric constant of the ring resonator, thus varying the resonant frequency of the ring resonator [42].

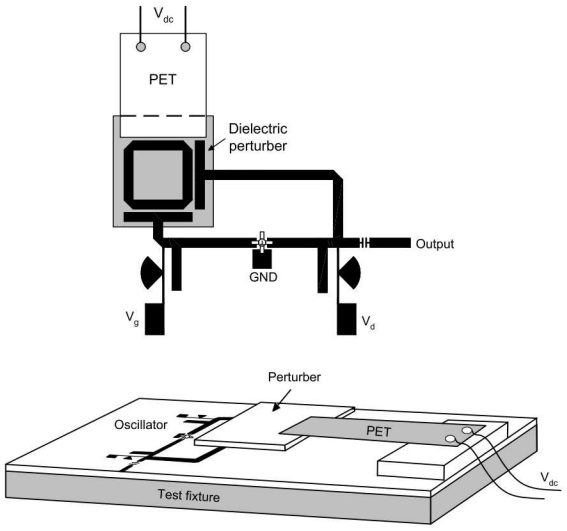

Figure 31
Configuration of the tunable oscillator using a PET: (a) top view; (b) 3D view [42]. (Permission from IEEE.)

Figure 32 shows the measured results of the oscillator using the PET tuning. The perturber attached on the PET has a dielectric constant of ε_r =10.8 and thickness of h=50 mil. The tuning range of the oscillator is from 11.49 GHz (at the applied voltage of +90 V to PET) with a power output of 3.17 dBm to 12 GHz (0 V) with a power output of 5.33 dBm.

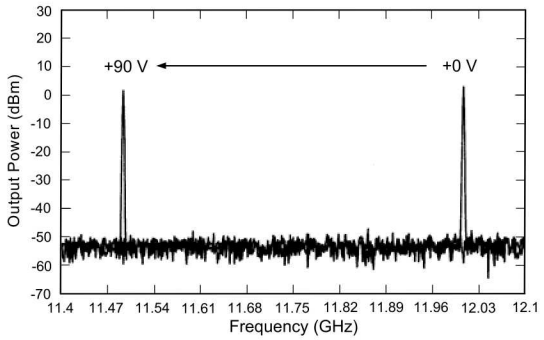

Figure 32
Measured tuning range of 510 MHz for the tunable oscillator using a PET [42]. (Permission from IEEE.)

8 Conclusions

A simple and useful ring resonator has been described. Because of its advantages of high Q, low radiation loss, low cost, and easy fabrication, it has been widely used in various applications such as dispersion measurement, filters, couplers, balanced mixers, balanced amplifiers, antennas, and oscillators. It is believed that many new applications could emerge in the future.

Bibliography

[1] P. Troughton, Measurement techniques in microstrip, *Electron. Lett.* **5**(2): 25–26 (Jan. 1969).

[2] I. Wolff and N. Knoppik, Microstrip ring resonator and dispersion measurements on microstrip lines, *Electron. Lett.* **7**(26): 779–781 (Dec. 1971).

[3] K. Chang, T. S. Martin, F. Wang, and J. L. Klein, On the study of microstrip ring and varactor-tuned ring circuits, *IEEE Trans. Microwave Theory Tech.* **35**: 1288–1295 (Dec. 1987).

[4] G. K. Gopalakrishnan and K. Chang, Bandpass characteristics of split-modes in asymmetric ring resonators, *Electron. Lett.* **26**(12): 774–775 (June 1990).

[5] L.-H. Hsieh and K. Chang, Equivalent lumped elements G, L, C, and unloaded Q's of closed- and open-loop ring resonators, *IEEE Trans. Microwave Theory Tech.* **50**(2): 453–460 (Feb. 2002).

[6] C. Ho, L. Fan, and K. Chang, New uniplanar coplanar waveguide hybrid-ring couplers and magic-Ts, *IEEE Trans. Microwave Theory Tech.*. **42**(12): 2440–2448 (Dec. 1994).

[7] J. A. Navarro, and K. Chang, Varactor-tunable uniplanar ring resonators, *IEEE Trans. Microwave Theory Tech.* **41**(5): 760–766 (May 1993).

[8] W. K. Hui and I. Wolff, Dielectric ring-gap resonator for application in MMIC's, *IEEE Trans. Microwave Theory Tech.* **39**(12): 2061–2068 (Dec. 1991).

[9] C. Ho, L. Fan, and K. Chang, A new type of waveguide ring cavity for resonator and filter applications, *IEEE Trans. Microwave Theory Tech.* **42**(1): 41–51 (Jan. 1994).

[10] K. Chang and L.-H. Hsieh, *Microwave Ring Circuits and Related Structures*, Wiley, New York, 2004.

[11] Y. S. Wu and F. J. Rosenbaum, Mode chart for microstrip ring resonators, *IEEE Trans. Microwave Theory Tech.* **21**: 487–489 (July 1973).

[12] R. P. Owens, Curvature effect in microstrip ring resonators, *Electron. Lett.* **12**(14): 356–357 (July 1976).

[13] S. G. Pintzos and R. Pregla, A simple method for computing the resonant frequencies of microstrip ring resonators, *IEEE Trans. Microwave Theory Tech.* **26**: 809–813 (Oct. 1978).

[14] L.-H. Hsieh and K. Chang, Simple analysis of the frequency modes for microstrip ring resonators of any general shape and the correction of an error in literature, *Microwave and Optical Technology Letters*, vol. 3, pp. 209-213 (June 2003).

[15] I. Wolff, Microstrip bandpass filter using degenerate modes of a microstrip ring resonator, *Electron. Lett.* **8**(12): 302–303 (June 1972).

[16] L. Zhu and K. Wu, A joint field/circuit model of line-to-ring coupling structures and its application to the design of microstrip dual-mode filters and ring resonator circuits, *IEEE Trans. Microwave Theory Tech.* **47**(10): 1938–1948 (Oct. 1999).

[17] L.-H. Hsieh and K. Chang, Compact dual-mode elliptic-function bandpass filter using a single ring resonator with one coupling gap, *Electron. Lett.* **36**(19): 1626–1627 (Sep. 2000).

[18] J. S. Hong and M. J. Lancaster, Bandpass characteristics of new dual-mode microstrip square loop resonators, *Electron. Lett.* **31**(11): 891–892 (May 1995).

[19] L.-H. Hsieh and K. Chang, Compact, low insertion-loss, sharp-rejection, and wide-band microstrip bandpass filters, *IEEE Trans. Microwave Theory Tech.* **51**(4): 1241–1246 (April 2003).

[20] L.-H. Hsieh and K. Chang, Tunable microstrip bandpass filters with two transmission zeros, *IEEE Trans. Microwave Theory Tech.* **51**(2): 520–525 (Feb. 2003).

[21] J. T. Kuo, M. J. Maa, and P. H. Lu, A microstrip elliptic function filter with compact miniaturized hairpin resonators, *IEEE Microwave Guided Wave Lett.* **10**(3): 94–95 (March 2000).

[22] L.-H. Hsieh and K. Chang, Microstrip dual-band bandpass filters using parallel-connected open-loop ring resonators, *International Journal of RF and Microwave Computer-Aided Engineering* , 219-224 (May 2008).

[23] IE3D Version 8.0, Zeland Software Inc., Fremont, CA, January 2001.

[24] P. Akkaraekthalin, S. Jongjitaree, and V. Vivek, Coplanar waveguide balanced amplifier using bipolar junction transistors and backed ground-plane hybrids, *Electrical and Electronic Tech., TENCON, International Conference*, Vol. **2**, pp. 732–735, 2001.

[25] H. R. Ahn and I. Wolff, Asymmetric ring-hybrid phase shifters and attenuators, *IEEE Trans. Microwave Theory Tech.* **50**(4): 1146–1155 (April 2002).

[26] X. Xie, J. Khurgin, J. Kang, and F. S. Choa, Ring-assisted frequency discriminator with improved linearity, *IEEE Photon. Tech. Lett.* **14**(8): 1136–1138 (Aug. 2002).

[27] K. Chang, D. M. English, R. S. Tahim, A. J. Grote, T. Phan, C. Sun, G. M. Hayashibara, P. Yen, and W. Piotrowski, W-band (75–110 GHz) microstrip components, *IEEE Trans. Microwave Theory Tech.* **33**(12): 1375–1382 (Dec. 1985).

[28] C. Y. Pon, Hybrid-ring directional couplers for arbitrary power division, *IRE Trans. Microwave Theory Tech.* **9**: 529–535 (Nov. 1961).

[29] S. March, A wideband stripline hybrid ring, *IEEE Trans. Microwave Theory Tech.* **16**: 361–369 (June 1968).

[30] R. R. Ramirez, F. DeFlaviis, and N. G. Alexopoules, Single-feed circularly polarized microstrip ring antenna and arrays, *IEEE Trans. Anten. Propag.* **48**(7): 1040–1047 (July 2000).

[31] T. K. Wu and S. W. Lee, Multiband frequency selective surface with multiring patch elements, *IEEE Trans. Anten. Propag.* **42**(11): 1484–1490 (Nov. 1994).

[32] C. M. Montiel, L. Fan, and K. Chang, Active-notch antennas stabilized with a slotline-ring resonator for wireless applications, *IEEE Trans. Anten. Propag.* **46**(6): 945–946 (June 1998).

[33] C. Han and K. Chang, Ka-band reflectarray using ring elements, *Electron. Lett.* **39**(6): 491–493 (March 2003).

[34] A. K. Bhattacharyya and R. Garg, Self and mutual admittance between two concentric, coplanar, circular radiating current sources, *Proc. IEE.* **130**(Part H)(6):217–219 (June 1984).

[35] K. D. Stephan, N. Camilleri, and T. Itoh, A quasi-optical polarization-duplexed balanced mixer for millimeter-wave applications, *IEEE Trans. Microwave Theory Tech.* **31**(2): 164–170 (Feb. 1983).

[36] H. Tehrani and K. Chang, Multifrequency operation of microstrip-fed slot-ring antennas on thin low-dielectric permittivity substrates, *IEEE Trans. Anten. Propag.* **50**(9): 1299–1308 (Sep. 2002).

[37] H. Tehrani and K. Chang, A multi-frequency microstrip-fed annular slot antenna, Proc. IEEE AP-S Int. Symp. Digest, July 2000, pp. 632–636.

[38] J. Huang and R. Pogorzelski, A Ka-band microstrip reflectarray with elements having variable rotation angles, *IEEE Trans. Anten. Propag.* **46**(5): 650–656 (May 1998).

[39] Y. D. Lee, M. H. Lee, K. H. Lee, W. P. Hong, and U. S. Hong, Voltage-controlled hair-pin resonator oscillator with new tuning mechanism, *Electron. Lett.* **36**(17): 1470–1471 (Aug. 2000).

[40] N. Popovic, Novel method of DRO frequency tuning with varactor diode, *Electron. Lett.* **26**(15): 1162 (July 1990).

[41] S. Qi, K. Wu, and Z. Ou, Hybrid integrated HEMT oscillator with a multiple-ring nonradiative dielectric (NRD) resonator feedback circuit, *IEEE Trans. Microwave Theory Tech.* **46**(10): 1552–1558 (Oct. 1998).

[42] L.-H. Hsieh and K. Chang, High-efficiency piezoelectric-transducer-tuned feedback microstrip ring-resonator oscillators operating at high resonant frequencies, *IEEE Trans. Microwave Theory Tech.* **51**(4): 1141–1145 (April 2003).

[43] F. X. Sinnesbichler, B. Hautz, and G. R. Olbrich, A Si/SiGe HBT dielectric resonator push–push oscillator at 58 GHz, *IEEE Microwave Guided Wave Lett.* **10**(4): 145–147 (April 2000).